

# Algorithms for numerically stable scattering amplitudes

Enrico Bothmann,<sup>1</sup> John M. Campbell,<sup>2</sup> Stefan Höche,<sup>2</sup> and Max Knobbe<sup>1</sup>

<sup>1</sup>*Institut für Theoretische Physik, Georg-August-Universität Göttingen, 37077 Göttingen, Germany*

<sup>2</sup>*Fermi National Accelerator Laboratory, Batavia, IL, 60510, USA*

The numerically stable evaluation of scattering matrix elements near the infrared limit of gauge theories is of great importance for the success of collider physics experiments. We present a novel algorithm that utilizes double-precision arithmetic and reaches higher precision than a naive quadruple-precision implementation at smaller computational cost. The method is based on physics-driven modifications to propagators, vertices and external polarizations.

During the past decades, particle physics experiments have explored the structure of matter and its interactions at an unprecedented pace and precision. We owe much of this scientific progress to the development of particle colliders [1]. The physics program at collider experiments depends critically on theoretical predictions based on the Standard Model of particle physics, which are typically obtained using perturbation theory [2].

At higher orders in the perturbative expansion, scattering matrix elements develop infrared singularities that arise from long-distance interactions between degenerate asymptotic states [3]. These infrared singularities lead to enormous complications in numerical calculations that rely on Monte-Carlo methods for the integration over phase space. They have become particularly problematic in the context of semi-automated computations at higher order in QCD, which are needed to realize the full physics potential of the Large Hadron Collider [4, 5]. At the next-to-leading order, calculations can be performed with the help of generic infrared subtraction methods [6]. A similar automation at the next-to-next-to leading order in QCD seems within reach [5]. All existing methods do, however, rely on the cancellation between real-emission matrix elements, and their corresponding approximations in the soft and collinear limits [7, 8]. Approaching the limit, the finite remainder can only be computed reliably if both the matrix elements and their approximations can be evaluated at high numerical accuracy *individually*.

It is often assumed that numerical stability issues in the computation of matrix elements are best addressed with the help of multiple precision arithmetic. In this letter, we will show that this is neither necessary nor sufficient. We propose a novel method that is computationally more efficient and also offers the opportunity to probe the deep infrared region through a suitable reformulation of the relevant components of tree-level matrix elements. While the details of a numerical implementation can be quite involved, the basic idea behind the method is simple: We express every part of the amplitude in terms of large and small components of four momenta. Quantities that become parametrically small in the infrared limits appear in most cases in the form of ratios of the small over the large momentum components, and such ratios can always be evaluated reliably. This is in stark contrast to a naive multiple-precision computation, where small quantities typically emerge as the difference

between components of four momenta that are individually large. At no point in the calculation does our new method involve any approximations. All expressions remain exact to the given order in perturbation theory.

## I. STABILITY PROBLEMS AND SOLUTIONS

Numerical imprecisions in tree-level matrix elements arise from multiple sources. The one that is most easily understood is the denominator of propagators in momentum space. For massless particles, it contains terms of the form  $1 - \cos\theta$ , which originate in the retarded Greens functions of the theory. In this context,  $\theta$  is the opening angle between the momentum of the particle emitting a gauge field quantum, and the momentum of the emission. Whether using Feynman graphs, or a recursive algorithm such as the Berends-Giele method [9], we need to find a numerically stable algorithm to compute such terms when  $\cos\theta \approx 1$ . This is relatively straightforward. The numerators of Feynman diagrams, which arise from the spin-dependence of the interactions, are harder to control. There are often intricate cancellations among different graphs, which are difficult to achieve numerically. To solve this problem, we will propose convenient expressions for the vertex factors and external wave functions, and make use of a physical gauge that suppresses interferences in the collinear limits [10].

### A. Scalar products and light-cone momenta

We begin by discussing a numerically stable algorithm to compute the invariant mass of a momentum vector  $q = p + k$ , which is given by  $q^2 = p^2 + k^2 + 2pk$ . The key idea is to represent each four-momentum in the numerical calculation as a five-vector, with the fifth component being the virtuality. If this virtuality is known to high precision, the task of finding  $q^2$  reduces to a computation of the scalar product,  $2pk$ . In anticipation of the expressions needed to evaluate vertex factors involving vector boson currents, we will discuss the most general case of complex four-momenta. The scalar product can be rewritten as

$$2pk = 2p_0k_0 \left[ 1 - \frac{\bar{p}\bar{k}}{p_0k_0} \right] + 2\bar{p}\bar{k} \left( 1 - \vec{v}_p\vec{v}_k \right), \quad (1)$$

where

$$\vec{v}_p = \frac{\vec{p}}{\bar{p}}, \quad \text{and} \quad \vec{v}_k = \frac{\vec{k}}{\bar{k}}. \quad (2)$$

The signed magnitudes of the momenta are defined as

$$\bar{p} = p_0 \sqrt{1 - \mu_p^2}, \quad \text{and} \quad \bar{k} = k_0 \sqrt{1 - \mu_k^2}, \quad (3)$$

where

$$\mu_p^2 = \frac{p^2}{p_0^2}, \quad \text{and} \quad \mu_k^2 = \frac{k^2}{k_0^2}. \quad (4)$$

The solutions of the square roots are taken such that the real part is maximized. Evaluating Eq. (3) in terms of  $\mu_p^2$  and  $\mu_k^2$  ensures that the velocities remain precise for (near) on-shell momenta. The difference  $1 - \vec{v}_p \vec{v}_k$  leads to large cancellations at small angles, which is one of the problems we aim to address. A numerically stable computation can be performed with the help of the identity [11, 12]

$$2(1 - \vec{v}_p \vec{v}_k) = (\vec{v}_p - \vec{v}_k)^2. \quad (5)$$

We are left to evaluate the difference in the square bracket of Eq. (1) as accurately as possible. This is achieved with the help of the following identity, again making use of the numerical stability of  $\mu_p^2$  and  $\mu_k^2$ ,

$$1 - \frac{\bar{p} \bar{k}}{p_0 k_0} = \frac{\mu_p^2 + \mu_k^2 - \mu_p^2 \mu_k^2}{1 + \sqrt{1 - \mu_p^2} \sqrt{1 - \mu_k^2}}. \quad (6)$$

In both vertices and propagators we often encounter terms of the form  $p_{\pm} = p_0 \pm p_z$ . In configurations with momenta collinear to the  $z$ -direction, the evaluation of such expressions necessitates a reformulation in terms of large and small components. This can be achieved using the following relation:

$$p_{\pm} = \begin{cases} p_0 \pm p_z & \text{if } |p_0 \pm p_z|^2 > |p_0 \mp p_z|^2 \\ & \text{or } |p_z|^2 < |p_{\perp}|^2 \\ \frac{p^2 + p_{\perp}^2}{p_0 \mp p_z} & \text{else} \end{cases}. \quad (7)$$

The condition  $|p_z|^2 < |p_{\perp}|^2$  is particularly relevant for the polarization vectors that will be introduced in Eq. (10). It is always fulfilled in the initial-state collinear regions.

In the deep infrared region of final-state collinear sectors of the phase space, it is not possible to store external momentum configurations at sufficient precision to allow for the reliable extraction of transverse or anti-parallel components relevant to collinear splittings. These components, and the related scalar invariants must be obtained from a phase-space generator which computes them directly in terms of the integration variables. Such

generators can be constructed based on any collinear phase-space parametrization, for example [6]. A convenient method for NNLO calculations was introduced in [13]. The supplemental material of this article discusses how it is used in our numerical tests. A high-precision evaluation of the matrix element then requires as input not only the momenta of the individual particles, but also their difference to the collinear direction and the invariants in the collinear sector.

## B. Wave functions of external states

The numerical stability of the external wave functions and their products with vertex factors often plays a key role in numerical computations. It is particularly important in initial- and final-state collinearly enhanced regions. The spinors of external fermions are typically constructed using the Weyl representation [14]

$$\begin{aligned} \chi_+(p) &= \begin{pmatrix} \sqrt{p_+} \\ \sqrt{p_-} e^{i\phi_p} \end{pmatrix}, \\ \chi_-(p) &= \begin{pmatrix} \sqrt{p_-} e^{-i\phi_p} \\ -\sqrt{p_+} \end{pmatrix}. \end{aligned} \quad (8)$$

These expressions are evaluated in a numerically stable fashion in a straightforward manner, by using Eq. (7) to compute the light-cone momenta  $p_+$  and  $p_-$ . The polarization vectors pose a slightly more difficult problem, due to their gauge dependence. In the helicity formalism [15], they contain a longitudinal component, which becomes problematic if the angle between the gauge vector<sup>1</sup> and the momentum is small. This can be made explicit by assuming a gauge vector of  $e_{\pm}^{\mu} = (1, 0, 0, \pm 1)$ , in which case the polarization vector for helicity  $\lambda$  is given by

$$\begin{aligned} \varepsilon_{\lambda}^{\mu}(p, e_{\pm}) &= \pm e^{-i\lambda\phi_p} \left[ \frac{p^{\pm}}{\sqrt{2p^+p^-}} e_{\pm}^{\mu} \right. \\ &\quad \left. + \frac{e^{\mp i\lambda\phi_p}}{\sqrt{2}} \left( e_x^{\mu} \pm i\lambda e_y^{\mu} \right) \right], \end{aligned} \quad (9)$$

with  $e_x^{\mu} = (0, 1, 0, 0)$ , and  $e_y^{\mu} = (0, 0, 1, 0)$ . One finds that the component along  $e_{\pm}^{\mu}$  diverges as  $\sqrt{p^{\pm}/p^{\mp}}$ . It is of course possible to remove this artifact by using a gauge vector,  $q$ , with  $(\vec{p}\vec{q})/(p_0q_0) < 0$ . Nevertheless, we propose a different definition based on real-valued three-vectors, due to its convenient numerical and analytical properties

$$\begin{aligned} \varepsilon_1^{\mu}(p) &= \left( 0, \frac{(\vec{n}\vec{p})\vec{p} - (p_0^2 - p^2)\vec{n}}{\sqrt{\vec{n}^2(p_0^2 - p^2) - (\vec{n}\vec{p})^2} \sqrt{p_0^2 - p^2}} \right), \\ \varepsilon_2^{\mu}(p) &= \left( 0, \frac{\vec{n} \times \vec{p}}{\sqrt{\vec{n}^2(p_0^2 - p^2) - (\vec{n}\vec{p})^2}} \right), \end{aligned} \quad (10)$$

<sup>1</sup> In the helicity formalism, the polarization vectors are given by  $\varepsilon_{\pm}^{\mu}(p, q) = \pm \langle q^{\mp} | \gamma^{\mu} | p^{\mp} \rangle / (\sqrt{2} \langle q^{\mp} | p^{\pm} \rangle)$ , with  $q^{\mu}$  the gauge vector.

where  $\vec{n}$  is  $\vec{e}_x$ ,  $\vec{e}_y$  or  $\vec{e}_z$ , depending on whether the largest component of the momentum is in  $x$ -,  $y$ - or  $z$ -direction. These real-valued polarizations can be used to define circular polarizations as  $\varepsilon_{\pm}^{\mu}(p) = (\varepsilon_1^{\mu}(p) \pm i\varepsilon_2^{\mu}(p))/\sqrt{2}$ .

### C. Vertices and propagators

When the individual components of a polarization vector are large compared to its virtuality, it becomes necessary to track the virtuality as an independent variable in the calculation. Scalar products with other currents are then evaluated using Eq. (1). Similarly, vertex factors involving light-cone momentum fractions should be computed using Eq. (7). Vertices involving fermions and fermion propagators are evaluated in the same fashion.

The computation of off-shell gluon currents [9] in the collinear region of phase space requires special methods in order to avoid numerical instabilities. Consider a pair of on-shell gluons with momenta  $p_a^{\mu}$  and  $p_b^{\mu}$  and polarization vectors  $\varepsilon_a^{\mu}$  and  $\varepsilon_b^{\mu}$ . The space-time dependent part of the corresponding two-particle current is generated by the triple-gluon vertex as follows:

$$\begin{aligned} \varepsilon_a^{\mu}\varepsilon_b^{\nu}\Gamma_{\mu\nu}{}^{\rho}(p_a, p_b, -p_{ab}) \\ = (\varepsilon_a\varepsilon_b)(p_a - p_b)^{\rho} + (2p_b\varepsilon_a)\varepsilon_b^{\rho} - (2p_a\varepsilon_b)\varepsilon_a^{\rho}, \end{aligned} \quad (11)$$

where  $p_{ab} = p_a + p_b$ . In the collinear limit  $p_a \parallel p_b$ , the last two terms are nearly transverse, because they are proportional to the one-particle currents. While formally transverse to  $p_{ab}$ , the first term, in fact, has a large longitudinal component that can be made explicit in a Sudakov decomposition [16]

$$\begin{aligned} p_a^{\mu} &= z_a\tilde{p}_{ab}^{\mu} + \frac{k_{\perp}^2 + p_a^2}{z_a 2\tilde{p}_{ab}n} n^{\mu} - k_{\perp}^{\mu}, \\ p_b^{\mu} &= z_b\tilde{p}_{ab}^{\mu} + \frac{k_{\perp}^2 + p_b^2}{z_b 2\tilde{p}_{ab}n} n^{\mu} + k_{\perp}^{\mu}. \end{aligned} \quad (12)$$

Here,  $n$  is an auxiliary, light-like vector that is linearly independent of the gluon momenta, and we have defined  $\tilde{p}_{ab}^{\mu} = p_{ab}^{\mu} - p_{ab}^2/(2p_{ab}n)n^{\mu}$ , as well as  $k_{\perp}^2 = -k_{\perp}^2$ . For practical applications, we choose  $n = (\sqrt{\tilde{p}_{ab}^2}, -\vec{p}_{ab})$ . To improve the numerical stability of Eq. (11), we perform the calculation in a light-like axial gauge, which is particularly suitable for collinear parton evolution [10]. In this gauge, the gluon polarization tensor reads

$$d^{\mu\nu}(p_{ab}, n) = -g^{\mu\nu} + \frac{p_{ab}^{\mu}n^{\nu} + n^{\mu}p_{ab}^{\nu}}{p_{ab}n}. \quad (13)$$

Multiplication by  $(p_a - p_b)^{\mu}$  from the first term of Eq. (11) yields the simple expression

$$d^{\mu\rho}(p_{ab}, n)(p_a - p_b)^{\rho} = 2k_{\perp}^{\mu} + (z_a - z_b)\frac{p_{ab}^2}{p_{ab}n}n^{\mu}. \quad (14)$$

Upon using the dedicated phase-space generator discussed earlier to parametrize the collinear limit, the values of  $k_{\perp}^{\mu}$  and  $p_{ab}^2$  are known to high precision.

Similar to the gluon currents, quark currents require a dedicated treatment in the collinear limit. Consider the product of propagator numerator and vertex factor for an on-shell quark,  $a$ , coupling to an on-shell gluon,  $b$ :

$$(\not{p}_a + \not{p}_b)\not{\varepsilon}_b u_a = (2p_a\varepsilon_b)u_a - i\sigma_{\mu\nu}p_b^{\mu}\varepsilon_b^{\nu}u_a. \quad (15)$$

The scalar interaction term can be evaluated using the methods described above. The magnetic term creates numerical instabilities of a different type. Using the Weyl representation of the  $\gamma$ -matrices, and the circular polarizations based on Eq. (10), we obtain

$$\begin{aligned} \frac{\sigma_{\mu\nu}p_b^{\mu}\varepsilon_b^{\nu}}{\sqrt{2}|p_{b\perp}|} &= \begin{pmatrix} 0 & 0 \\ 0 & \begin{vmatrix} 1 & -p_b^+/p_{b\perp} \\ p_{b\perp}/p_b^+ & -1 \end{vmatrix} \end{pmatrix}, \\ \frac{\sigma_{\mu\nu}p_b^{\mu}\varepsilon_b^{\nu}}{\sqrt{2}|p_{b\perp}|} &= \begin{pmatrix} -1 & -p_b^*/p_b^+ \\ p_b^+/p_b^* & 1 \end{vmatrix} \begin{vmatrix} 0 \\ 0 \end{vmatrix}. \end{aligned} \quad (16)$$

In the exact collinear limit,  $p_a = z_a p_{ab}$ ,  $p_b = z_b p_{ab}$ , the products of these matrices and the Dirac spinors derived from Eq. (8) vanish. Numerically precise results in final-state collinear regions can therefore only be obtained by expressing  $\sigma_{\mu\nu}p_b^{\mu}\varepsilon_b^{\nu}u_a$  in terms of Sudakov variables similar to Eq. (12), but separating the transverse momentum,  $k_{\perp}$ , into a component,  $k_{\perp}^+$ , which is parallel to the  $z$ -axis, and a remainder in the transverse plane.

## II. EXAMPLE APPLICATION: LHC PHYSICS

We demonstrate the utility of our method using tree-level matrix elements for Drell Yan lepton-pair production in association with two jets. The reference value is obtained from a calculation in arbitrary precision arithmetic with 256 significant digits, using the `mp++` library [17]. Figure 1 compares the achieved precision relative to the target from this implementation in the double-soft, triple-collinear and double-collinear limits. We adopt the scaling procedure described in the supplemental material of this article, which relies on the phase-space parametrization of [13].

In order to gauge the numerical stability of our algorithms in a practical calculation, we perform a computation of the  $u\bar{u}$  contribution to the NNLO correction,  $\delta\sigma_{\text{NNLO}}$ , in Drell-Yan lepton pair production at the LHC at  $\sqrt{s} = 13$  TeV. We use the PDF4LHC15+LUXqed NNLO PDF set [18], and the corresponding definition of the strong coupling. The electroweak parameters are defined as  $\sin^2\theta_W = 0.2223$  and  $\alpha = 1/128.89$ . We set  $m_Z = 91.1876$  GeV and  $\Gamma_Z = 2.4952$  GeV. The final-state electrons are required to fulfill  $66 \text{ GeV} \leq m_{e^+e^-} \leq 116$  GeV. Table I shows the results for  $\delta\sigma_{\text{NNLO}}$  in the  $u\bar{u}$  channel, computed using jettiness slicing [19]. The results labeled ‘‘BG recursion’’ are obtained with a combination of MCFM [19, 20] and Pepper [21], all other results stem from MCFM. The uncertainty on the results

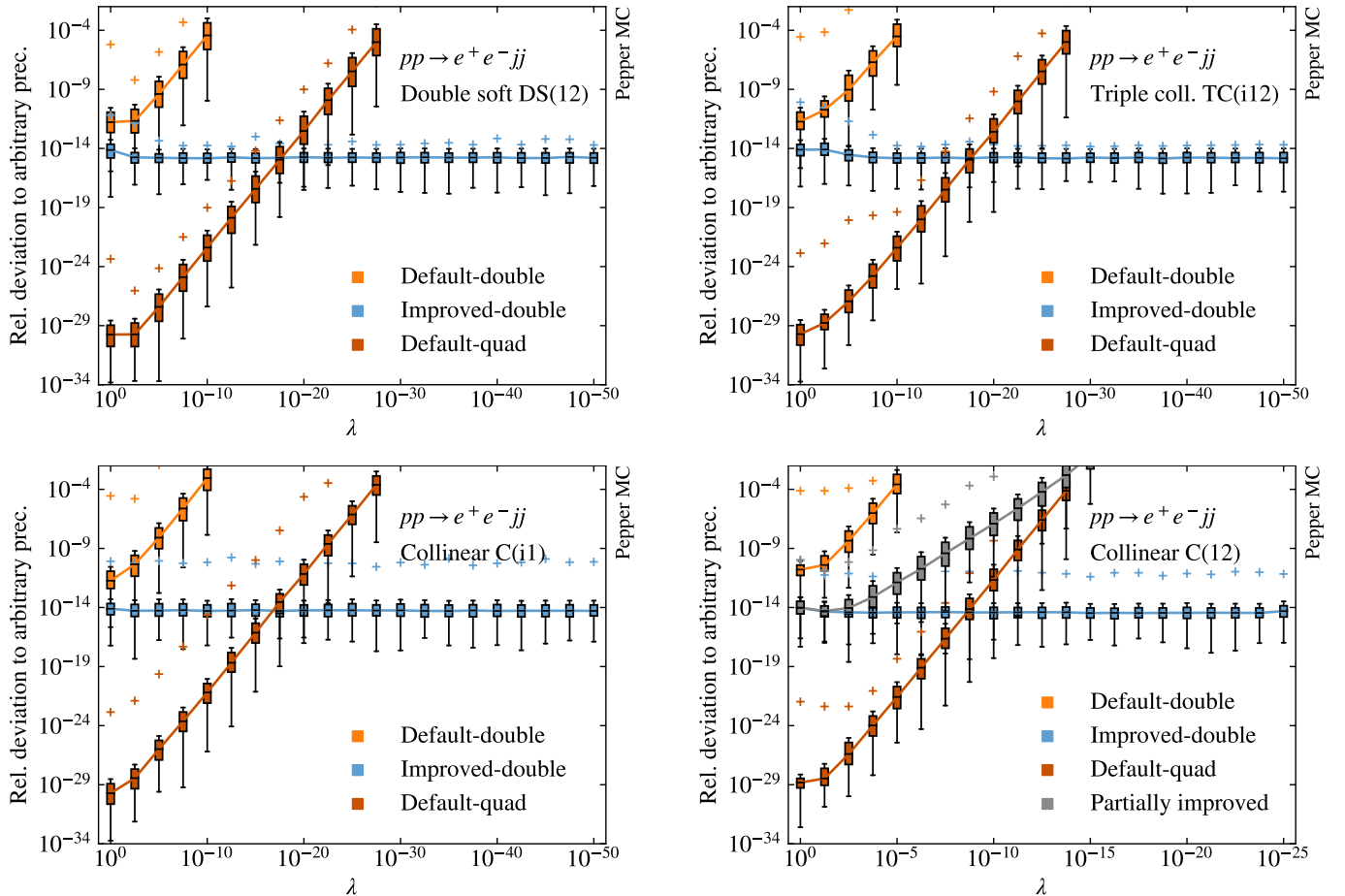


FIG. 1. Relative precision of the matrix-element computation as a function of the scaling parameter,  $\lambda$  (see supplemental material), in the double-soft (top left), triple-collinear (top right), initial-state double-collinear (bottom left) and final-state double-collinear (bottom right) limit. We compare a naive double precision (orange), naive quadruple precision (red) and improved double precision (blue) implementation. The box plots are obtained from  $10^4$  phase-space trajectories constructed as described in the supplemental material. The boxes show the quartiles of the distribution, the whiskers indicate  $3/2$  of the interquartile range, and the crosses mark the maximum values. The grey distribution shows the improvements obtained in final-state collinear regions without a Sudakov decomposition of the spin-dependent part of interaction vertices.

$\tau_{\text{cut}}$	$\delta\sigma_{\text{NNLO}}(u\bar{u} \rightarrow e^+e^- + X)$ [pb]		
	naive double	improved double	
		analytic ME	BG recursion
$10^{-2}$	28.11(5)	28.12(5)	28.10(7)
$10^{-3}$	27.4(3)	27.0(1)	27.0(1)
$10^{-4}$	27.2(4)	27.4(3)	27.0(3)
$10^{-5}$	-	27.2(9)	27.1(8)
$10^{-6}$	-	27.7(18)	27.4(16)

TABLE I. Contribution of the  $u\bar{u}$  initial state to the NNLO correction in  $pp \rightarrow e^+e^-$  at  $\sqrt{s} = 13$  TeV. See the main text for details.

is driven by the subtracted real emission corrections, for which we employ the techniques described before, both in the real-emission matrix element, and in all associated infrared counterterms. The calculation reported in ta-

ble I should be independent of the parameter  $\tau_{\text{cut}}$  in the limit  $\tau_{\text{cut}} \rightarrow 0$  and in practice one must choose a value of  $\tau_{\text{cut}}$  that is deemed to be in the asymptotic region. The naive double precision implementation fails below  $\tau_{\text{cut}} \approx 10^{-4}$ , leaving only two data points to support this assertion. It is therefore not clear whether the result is correct. The improved implementation remains usable down to  $\tau_{\text{cut}} \approx 10^{-6}$ , and its results demonstrate that the asymptotic region has indeed been reached. The total additional computing time expended in our unoptimized code is 5% for MCFM, and 80% for MCFM+Pepper. We expect a reduction of this overhead in an optimized implementation.

### III. CONCLUSIONS

This letter discussed a simple set of physics-driven algorithms to stabilize the computation of tree-level

matrix elements needed for precision physics at colliders. The methods are applicable to both analytically computed matrix elements and fully numerical approaches. We have presented example numerical results and demonstrated the utility of the technique for precision physics. In view of the increased statistics and reduced experimental systematics in the upcoming high-luminosity phase of the Large Hadron Collider, the improvements discussed here will be of utmost importance for the extraction of Standard Model parameters from experimental measurements.

This research was supported by the Fermi National Accelerator Laboratory (Fermilab), a U.S. Department

of Energy, Office of Science, HEP User Facility managed by Fermi Research Alliance, LLC (FRA), acting under Contract No. DE-AC02-07CH11359. The work of J.M.C. and S.H. was supported by the U.S. Department of Energy, Office of Science, Office of Advanced Scientific Computing Research, Scientific Discovery through Advanced Computing (SciDAC-5) program, grant “NeuCol”. E.B. and M.K. acknowledge support from BMBF (contract 05H21MGCAB). Their research is funded by the Deutsche Forschungsgemeinschaft (DFG) – 456104544; 510810461. We used resources of the National Energy Research Scientific Computing Center (NERSC), a U.S. Department of Energy Office of Science User Facility using NERSC awards HEP-ERCAP0023824 and HEP-ERCAP0028985.

- 
- [1] R. K. Ellis *et al.*, (2019), arXiv:1910.11775 [hep-ex]; J. N. Butler *et al.*, (2023), 10.2172/1922503.
- [2] M. Narain *et al.*, (2022), arXiv:2211.11084 [hep-ex]; N. Craig *et al.*, (2022), arXiv:2211.05772 [hep-ph].
- [3] F. Bloch and A. Nordsieck, Phys. Rev. **52**, 54 (1937); D. R. Yennie, S. C. Frautschi, and H. Suura, Annals Phys. **13**, 379 (1961); T. Kinoshita, J. Math. Phys. **3**, 650 (1962); T. D. Lee and M. Nauenberg, Phys. Rev. **133**, B1549 (1964).
- [4] G. Heinrich, Phys. Rept. **922**, 1 (2021), arXiv:2009.00516 [hep-ph]; F. Febres Cordero, A. von Manteuffel, and T. Neumann, Comput. Softw. Big Sci. **6**, 14 (2022), arXiv:2204.04200 [hep-ph].
- [5] A. Huss, J. Huston, S. Jones, and M. Pellen, J. Phys. G **50**, 043001 (2023), arXiv:2207.02122 [hep-ph].
- [6] S. Frixione, Z. Kunszt, and A. Signer, Nucl. Phys. B **467**, 399 (1996), hep-ph/9512328; S. Catani and M. H. Seymour, Nucl. Phys. B **485**, 291 (1997), [Erratum: Nucl.Phys.B 510, 503–504 (1998)], hep-ph/9605323; S. Catani, S. Dittmaier, M. H. Seymour, and Z. Trocsanyi, Nucl. Phys. B **627**, 189 (2002), hep-ph/0201036.
- [7] A. H. Mueller, Phys. Lett. **B104**, 161 (1981); B. I. Ermolaev and V. S. Fadin, JETP Lett. **33**, 269 (1981); Y. L. Dokshitzer, V. S. Fadin, and V. A. Khoze, Phys. Lett. B **115**, 242 (1982); Z. Phys. **C15**, 325 (1982); A. Bassetto, M. Ciafaloni, G. Marchesini, and A. H. Mueller, Nucl. Phys. **B207**, 189 (1982); A. Bassetto, M. Ciafaloni, and G. Marchesini, Phys. Rept. **100**, 201 (1983).
- [8] Y. L. Dokshitzer, Sov. Phys. JETP **46**, 641 (1977); V. N. Gribov and L. N. Lipatov, Sov. J. Nucl. Phys. **15**, 438 (1972); L. N. Lipatov, **20**, 94 (1975); G. Altarelli and G. Parisi, Nucl. Phys. **B126**, 298 (1977).
- [9] F. Berends and W. Giele, Nuclear Physics B **306**, 759 (1988); F. A. Berends, W. T. Giele, and H. Kuijff, Nucl. Phys. B **321**, 39 (1989); F. A. Berends, H. Kuijff, B. Tausk, and W. T. Giele, Nucl. Phys. B **357**, 32 (1991).
- [10] D. Amati, R. Petronzio, and G. Veneziano, Nucl. Phys. B **140**, 54 (1978); Nucl. Phys. B **146**, 29 (1978); R. K. Ellis, H. Georgi, M. Machacek, H. D. Politzer, and G. G. Ross, Phys. Lett. B **78**, 281 (1978); Nucl. Phys. B **152**, 285 (1979); J. Kalinowski, K. Konishi, and T. R. Taylor, Nucl. Phys. B **181**, 221 (1981); J. Kalinowski, K. Konishi, P. N. Scharbach, and T. R. Taylor, Nucl. Phys. B **181**, 253 (1981); J. F. Gunion, J. Kalinowski, and L. Szymanowski, Phys. Rev. D **32**, 2303 (1985); S. Catani and M. Grazzini, Nucl. Phys. B **570**, 287 (2000), hep-ph/9908523.
- [11] W. Kahan, in *Proc. Householder Symposium XVI on Numerical Linear Algebra* (2005).
- [12] W. Kahan, (2006), How Futile are Mindless Assessments of Roundoff in Floating-Point Computation? (unpublished).
- [13] M. Czakon, Phys. Lett. B **693**, 259 (2010), arXiv:1005.0274 [hep-ph]; Nucl. Phys. B **849**, 250 (2011), arXiv:1101.0642 [hep-ph]; F. Caola, K. Melnikov, and R. Röntsch, Eur. Phys. J. C **77**, 248 (2017), arXiv:1702.01352 [hep-ph]; K. Asteriadis, Ph.D. thesis, KIT, Karlsruhe, EKP (2021).
- [14] L. J. Dixon, (1996), hep-ph/9601359; S. Dittmaier, Phys. Rev. D **59**, 016007 (1998), hep-ph/9805445.
- [15] F. A. Berends, R. Kleiss, P. De Causmaecker, R. Gastmans, and T. T. Wu, Phys. Lett. B **103**, 124 (1981); P. De Causmaecker, R. Gastmans, W. Troost, and T. T. Wu, Nucl. Phys. B **206**, 53 (1982); R. Kleiss and W. J. Stirling, Nucl. Phys. B **262**, 235 (1985); Z. Xu, D.-H. Zhang, and L. Chang, Nucl. Phys. B **291**, 392 (1987); J. F. Gunion and Z. Kunszt, Phys. Lett. B **161**, 333 (1985).
- [16] V. V. Sudakov, Sov. Phys. JETP **3**, 65 (1956).
- [17] F. Biscani, D. Izzo, A. Corrigan, and T. G. Badger, “bluescarni/mppp: mp++ 1.0.2,” (2023).
- [18] J. Butterworth *et al.*, J. Phys. G **43**, 023001 (2016), arXiv:1510.03865 [hep-ph]; A. V. Manohar, P. Nason, G. P. Salam, and G. Zanderighi, JHEP **12**, 046 (2017), arXiv:1708.01256 [hep-ph].
- [19] R. Boughezal, J. M. Campbell, R. K. Ellis, C. Focke, W. Giele, X. Liu, F. Petriello, and C. Williams, Eur. Phys. J. C **77**, 7 (2017), arXiv:1605.08011 [hep-ph]; J. Campbell and T. Neumann, JHEP **12**, 034 (2019), arXiv:1909.09117 [hep-ph].
- [20] J. M. Campbell, R. K. Ellis, and W. T. Giele, Eur. Phys. J. C **75**, 246 (2015), arXiv:1503.06182 [physics.comp-ph].
- [21] E. Bothmann, T. Childers, W. Giele, S. Höche, J. Isaacson, and M. Knobbe, (2023), arXiv:2311.06198 [hep-ph].
- [22] E. Bothmann *et al.*, SciPost Phys. **7**, 034 (2019).

## Supplemental Material: Algorithms for numerically stable scattering amplitudes

### A. Scaling procedure

To generate the phase-space trajectories approaching the infrared limits relevant to NNLO calculations, we use the phase-space parametrization of [13]. The construction starts with a hard momentum,  $p_i$ , which defines the collinear direction. The momenta of up to two emissions,  $p_1$  and  $p_2$ , can be written as

$$\begin{aligned} p_1^\mu &= t^\mu + \cos \theta_{i1} e_i^\mu + \sin \theta_{i1} b^\mu, \\ p_2^\mu &= t^\mu + \cos \theta_{i2} e_i^\mu + \sin \theta_{i2} (\cos \phi b^\mu + \sin \phi a^\mu), \end{aligned} \quad (\text{S1})$$

where  $t^\mu = (1, \vec{0})$ ,  $e_i^\mu = (0, \vec{p}_i/|\vec{p}_i|)$ ,  $b^\mu$  is transverse to  $t^\mu$  and  $e_i^\mu$ , and  $a^\mu$  is transverse to  $t^\mu$ ,  $e_i^\mu$  and  $b^\mu$ . The construction of the transverse vectors is achieved as follows

$$b^\mu = \frac{\tilde{b}^\mu}{\sqrt{-\tilde{b}^2}}, \quad \text{where} \quad \tilde{b}^\mu = \sum_{k=1,3} \varepsilon^\mu_{\nu\rho k} e_i^\nu t^\rho, \quad \text{and} \quad a^\mu = \varepsilon^\mu_{\nu\rho\sigma} b^\nu e_i^\rho t^\sigma. \quad (\text{S2})$$

One defines the angular variables

$$\eta_{1/2} = \eta_{i1/i2} = \frac{1 - \cos \theta_{i1/i2}}{2} \quad \text{and} \quad \eta_{12} = \frac{1 - \cos \theta_{12}}{2}. \quad (\text{S3})$$

In terms of the azimuthal angle  $\phi_{12}$ , the variable  $\eta_{12}$  is given by

$$\eta_{12} = \eta_1 + \eta_2 - 2\eta_1\eta_2 - 2\cos \phi_{12} \sqrt{\eta_1(1-\eta_1)\eta_2(1-\eta_2)}. \quad (\text{S4})$$

A naive parametrization of the azimuthal integral would be given by  $\cos \phi_{12} = 1 - 2\xi$ . However, in order to disentangle the singularities at small  $\eta_{1/2}$  and small  $\eta_{12}$ , one uses instead [13]

$$\zeta = \frac{1 - \xi}{1 + 2\xi X}, \quad \text{where} \quad X = \left[ \frac{\eta_1 + \eta_2 - 2\eta_1\eta_2}{2\sqrt{\eta_1(1-\eta_1)\eta_2(1-\eta_2)}} - 1 \right]^{-1}, \quad (\text{S5})$$

such that

$$\eta_{12} = \frac{(\eta_1 - \eta_2)^2}{\eta_1 + \eta_2 - 2\eta_1\eta_2 - 2(1 - 2\zeta)\sqrt{\eta_1(1-\eta_1)\eta_2(1-\eta_2)}}, \quad \sin^2 \phi_{12} = 4\zeta(1 - \zeta) \frac{\eta_{12}^2}{(\eta_1 - \eta_2)^2}. \quad (\text{S6})$$

Starting with a set of phase-space points produced by a diagram-based phase-space generator [22], and a set of indices corresponding to  $i$ , 1 and 2, we order the indices such that the momenta satisfy  $E_2 < E_1$ . We then determine the angles  $\eta_{1/2}$ ,  $\xi$ , and the transverse vectors  $a^\mu$  and  $b^\mu$ . We map the energies and angles to the parameters  $x_{1/2}$  and  $x_{3/4}$ , using  $E_1 = x_1 E_{\max}$ ,  $E_2 = x_1 x_2 E_{\max}$ , and one of the following angular parametrizations [13]:

$$\begin{aligned} \text{Sector (a):} \quad \eta_1 &= x_3, \quad \eta_2 = \frac{x_3 x_4}{2}, & \text{Sector (b):} \quad \eta_1 &= x_3, \quad \eta_2 = x_3 \left(1 - \frac{x_4}{2}\right), \\ \text{Sector (c):} \quad \eta_2 &= x_3, \quad \eta_1 = \frac{x_3 x_4}{2}, & \text{Sector (d):} \quad \eta_2 &= x_3, \quad \eta_1 = x_3 \left(1 - \frac{x_4}{2}\right). \end{aligned} \quad (\text{S7})$$

There is exactly one such mapping for each phase-space point. We can then scale the original point into the soft ( $S$ ), double soft ( $DS$ ), double collinear ( $C$ ), and triple collinear ( $TC$ ) limits by redefining the variables  $x_1$  through  $x_4$ , and reconstructing the original point using the new variables. The possible options for rescaling are listed in Tab. I. They can be combined in order to test strongly ordered regions. For example, the combination  $C(12)DS(12)$  corresponds to the collinear limit of a double-soft (12) particle pair. Note that in the double-collinear limit,  $x_4 \rightarrow 0$ , the angular variable  $\eta_{12}$  in sectors (b) and (d) is proportional to  $x_4^2$ , such that the 12-collinear limit is approached twice as fast as the  $i1$  and  $i2$  collinear limits in sectors (a) and (c). As intended in the original publications [13], the above algorithm can also be used directly as a phase-space generator for collinear configurations.

Limit	Scaling	Sector	Limit	Scaling	Sector
$S(2)$	$x_2 \rightarrow \lambda$	any	$DS(12)$	$x_1 \rightarrow \lambda$	any
$C(i1)$	$x_4 \rightarrow \lambda$	(a)	$TC(i12)$	$x_3 \rightarrow \lambda$	any
$C(i2)$	$x_4 \rightarrow \lambda$	(c)	$C(12)$	$x_4 \rightarrow \lambda$	(b) or (d)

TABLE I. Scaling of the phase-space parameters in Eq. (S7) in the soft ( $S$ ), double soft ( $DS$ ), double collinear ( $C$ ), and triple collinear ( $TC$ ) limits. The above limits can be combined into strongly ordered limits by scaling two parameters.

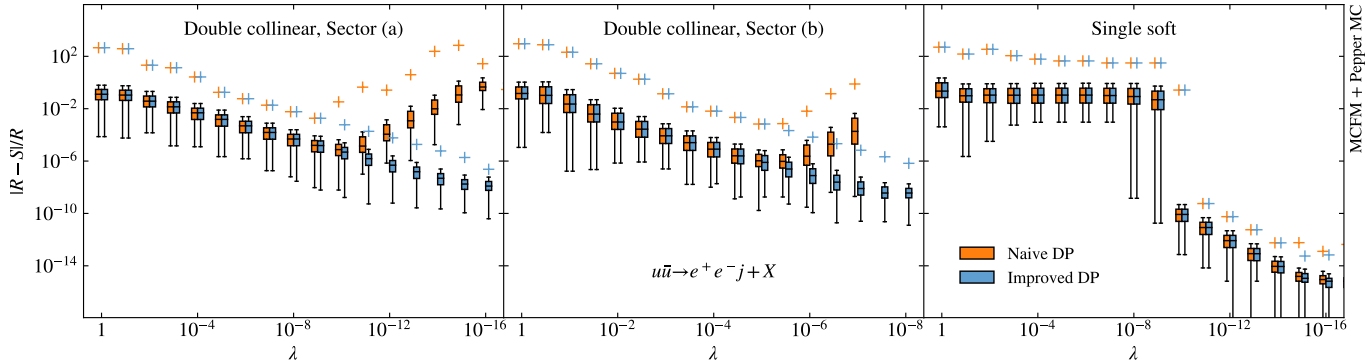


FIG. S1. Absolute value of the relative difference between the infrared subtraction terms and the real-emission matrix elements as a function of the scaling parameters,  $\lambda$ . We compare a naive double precision implementation (Naive DP) and the improved algorithm (Improved DP). The boxes show the median and quartiles of the distribution in  $10^4$  phase-space trajectories, the whiskers indicate  $3/2$  of the interquartile range and the crosses show the maximum values. For details see the main text.

## B. Infrared subtracted real-emission corrections

In this subsection we discuss the numerical precision of infrared subtracted real-emission QCD corrections at NLO that can be achieved with our new algorithms. We make use of the Catani-Seymour dipole method [6]. When evaluating the corresponding dipole subtraction terms, it is important to use the stable methods for computation of all potentially small dot products in the dipole insertion operators. Moreover, terms such as  $1 - z$  should be evaluated as a whole in terms of dot products whenever  $z$  can be large. These modifications are straightforward. The only nontrivial adaptation concerns the four-vectors which are used to evaluate the transverse momentum dependent parts of the gluon splitting functions. They are defined for final-final (FF), final-initial (FI), initial-final (IF) and initial-initial (II) dipoles in Eqs. (5.8), (5.41), (5.67) and (5.147) of Ref. [6], respectively:

$$k_{\perp, \text{FF/FI}}^{\mu} = \frac{\tilde{z}_i p_i^{\mu} - \tilde{z}_j p_j^{\mu}}{\sqrt{\tilde{z}_i \tilde{z}_j} 2p_i p_j}, \quad \text{and} \quad k_{\perp, \text{IF/II}}^{\mu} = \sqrt{\frac{p_i p_a p_k}{2p_i p_k}} \left( \frac{p_i^{\mu}}{p_i p_a} - \frac{p_k^{\mu}}{p_k p_a} \right). \quad (\text{S8})$$

These vectors are formally transverse to the emitter momenta,  $\tilde{p}_{ij}$  and  $\tilde{p}_a$ , and normalized to  $k_{\perp}^2 = -1$ . However, a Sudakov decomposition reveals that they contain a non-vanishing component in the direction of the emitter, and that this component diverges in the collinear limit, due to the normalization. Current conservation in the on-shell matrix elements eliminates terms proportional to  $\tilde{p}_{ij}^{\mu}$  and  $\tilde{p}_a^{\mu}$  in the insertion operators, however, numerically this is achieved through large cancellations in scalar products of near collinear momenta. We use an axial gauge to remove the longitudinal components in  $k_{\perp}^{\mu}$  explicitly, which corresponds to subtracting  $(\tilde{z}_i - \tilde{z}_j) \tilde{p}_{ij}^{\mu} / \sqrt{\tilde{z}_i \tilde{z}_j} 2p_i p_j$  in final-state dipoles, and  $\sqrt{p_a p_k / (2p_i p_k p_i p_a)} (1 - x) p_a^{\mu}$  in initial-state dipoles. This method stabilizes the calculation at  $\lambda \lesssim 10^{-9}$ .

Figure S1 shows tests of the cancellation between the dipole subtraction terms and the real-emission correction in the  $u\bar{u}$  initial state contribution to the NNLO double-real correction above  $\tau_{\text{cut}} = 10^{-6}$  in the jettiness slicing approach. The plots are obtained from  $10^4$  phase-space points, which are scaled according to the procedure described above. The left panel shows the behavior in the initial-state double collinear limit, the middle panel in the final-state double collinear limit, and the right panel in the single soft limit. We find that our improved numerical algorithms allow to probe the infrared region in much more detail than previously possible. The ledge in the right plot is due to dipole subtraction terms corresponding to the soft limit on gluon 1 when the momentum of gluon 2 is scaled to zero. These terms exhibit a soft scaling, leading to a constant offset in Fig. S1 for  $\tau(\{\tilde{p}\}) > \tau_{\text{cut}}$ .